Supporting Information

# Ultra-low Content Induced Intercalation Anomaly of Graphite Anode Enables Superior Capacity at Sub-zero Temperatures

*Febri Baskoro,[a,b] Po-Yu Yang,[c] Hong-Jhen Lin,[a] Robin Chih-Hsing Wang,[d] Hui Qi Wong,[a] Hsinhan Tsai,[e] Chun-Wei Pao,*[,c] Heng-Liang Wu,*[d,f] and Hung-Ju Yen,*[a]*

[a] Institute of Chemistry, Academia Sinica, 128 Academia Road, Section 2, Nankang, Taipei 11529, Taiwan.

[b] Material Science and Engineering Research Group, Faculty of Mechanical and Aerospace Engineering, Institut Teknologi Bandung, Jl. Ganesha 10, Bandung 40132, Indonesia

[c] Research Center for Applied Sciences, Academia Sinica, Taipei 11529, Taiwan.

[d] Center for Condensed Matter Sciences, National Taiwan University, Taipei 10617, Taiwan.

[e] Department of Chemical and Biological Engineering, The State University of New York at Buffalo, Buffalo, NY14260, USA

[f] Center of Atomic Initiative for New Materials, National Taiwan University, Taipei, 10617, Taiwan.

E-mail: cwpao@gate.sinica.edu.tw; hengliangwu@ntu.edu.tw; hjyen@gate.sinica.edu.tw

**Supplementary Notes:**

**Supplementary Note 1 - Diffusion coefficient calculation based on GITT method**

The galvanostatic intermittent titration technique (GITT) has been carried out to probe the ion diffusivity of the graphite anodes. The GITT measurement was performed using Squitstat potentiostats, an Admiral instrument, by alternating current density of 0.1C (1C = 372 mA h $g^{-1}$) for 20 min with a rest interval of 10 min. Prior to the GITT measurement, fresh coin cells were fully charged under 0.1C and allowed to rest for up to 10 hours. The diffusion coefficient was then calculated by the following formula :

$$D = \frac{4}{\pi\tau}\left(\frac{m_B V_M}{M_B S}\right)^2 \left(\frac{\Delta E_s}{\Delta E_t}\right)^2$$

Where $D$ is the diffusion coefficient ($cm^2\ s^{-1}$), $\tau$ is the current pulse (s), $m_B$ is the mass of the host material in the electrode (g), $V_M$ is the molar volume of the material ($cm^3\ mol^{-1}$), $M_B$ is the molecular weight of the host material (g $mol^{-1}$), and $S$ is the contact area of the electrolyte and electrode interface ($cm^2$). $\Delta E_s$ And $\Delta E_t$ are the voltage responses over the relaxation and current pulse, respectively.

**Supplementary Note 2 - Sweep rate voltammetry technique for capacitive contribution**

In the battery system, there are consecutive electrochemical reactions occurs in the electrodes. The sweep rate voltammetry is one of powerful technique to probe those reactions. The total stored charge in a CV curve generally can be separate into three components: (a) the faradaic contribution from the $Li^+$ ion insertion process; (b) the faradaic contribution from the charge-transfer process with surface atoms, referred to as pseudocapacitance; (c) the non-faradaic contribution from the double layer effect.[1, 2]

In addition, the contribution of both types capacitive effects, pseudocapacitance and double layer effect, can be substantial due to the increasing surface area of the electrode.[1] These faradaic contribution from insertion process (diffusion control) and capacitive effects can be characterized using CV data at various scan rates and expressed by following formula:

$$i = av^b$$

where *i* is current response to the scan rate *v*, while *a* and *b* are constants. The *b* value can be obtained from the slope of *log i* vs *log v*. In addition, if the *b* value close to 0.5 would indicate half-infinite linear diffusion controlled process, meanwhile *b* value close to 1 indicates the current is surface controlled.[1, 3-5] Since the *b* value is the sum of faradaic response of diffusion controlled and capacitive effects, a closer examination from sweep rate voltammetry can be applied to quantify the capacitive effects ($k_1v$) and diffusion controlled behavior ($k_2v^{1/2}$) by following formula:[1, 2, 4, 6]

$$i = k_1 v + k_2 v^{1/2}$$

The $k_1$ and $k_2$ values can be determined by plotting $i/v^{1/2}$ vs $v^{1/2}$.

**Supplementary Note 3 – Theoretical capacity**

In the battery system, the theoretical capacity of any active material can be estimated by Faraday' law:

$$Q = \frac{nF}{3.6M_w}$$

where, *n* is number electron transferred, *F* is Faraday constant, and $M_w$ is molecular weight of active material. According to Faraday's law, the theoretical capacity of $LiC_6$ and $LiC_2$ were estimated to be 372 and 1117 mA h $g^{-1}$. Surprisingly, the specific capacitity of **G10** is obtained about 2200 mA h $g^{-1}$ at room temperature, which is almost *six times* of conventional graphite capacity ($LiC_6$). Based on the sweep rate cyclic voltammetry measurement, the **G10** demonstrated a positive *b* value nearly 0.6 (see Fig. 5e). Further analysis of *b* value revealed a positive slope of $k_1$ (0.1742) and almost 40% contribution from capacitive effects in the **G10** electrode at higher scan rate of 0.7 mV $s^{-1}$(see Fig. 5f). Therefore, if we assume that the highest capacity of **G10** (2200 mA h $g^{-1}$) is generated from the contribution of both pseudocapacitive and diffusion controlled process (intercalation), a total capacity of ~880 mA h $g^{-1}$ (40%) can be counted as a resulted from capacitive behavior and ~1320 mA h $g^{-1}$ (60%) contributed from diffusion controlled process (intercalation). Hence, it suggest that a maximum capacity of 1320 mA h $g^{-1}$ is achieved via Li intercalation in between interlayer of graphite, which is close to the formation of $LiC_2$.

**Supplementary Note 4 - Diffusion coefficient calculation based on EIS spectra**

EIS is a powerful tool to investigate electrical properties of materials surface in association with physicochemical processes such as charge transfer of electronic and ionic charge carriers, mass transport through diffusion and convection.[7] The Nyquist plots typically can be divided into three sections, namely high, mid and low frequency regions. The high frequency region reflected the conduction through electrolyte, separator and wires.[8] The mid frequency region is related to the charge transfer and the kinetic reactions.[9, 10] The low frequency region in which usually featured by 45° slope, represents the diffusion limited region in the solid phase and is typically characterized by the Warburg impedance.[11, 12] Basically, there are two equations that define Warburg impedance:[13]

$$Z' = \sigma/\omega^{\frac{1}{2}} - j\,\sigma/\omega^{\frac{1}{2}}$$

$$\left| -Z'' \right| = \sqrt{2}\,\sigma/\omega^{\frac{1}{2}}$$

where Z′ and Z′′are real and imaginary impedance, respectively. ω is the angular frequency and σ is the Warburg coefficient. Therefore, The Warburg coefficient (σ) can be determine by the slope of Warburg plot (Z′ vs $1/\omega^{\frac{1}{2}}$). Meanwhile, the relationship of Warburg coefficient (σ) and the diffusion coefficient is given by:[13]

$$\sigma = \frac{RT}{n^2F^2A\sqrt{2}}\left(\frac{1}{D_O^{\frac{1}{2}}C_O^b} + \frac{1}{D_R^{\frac{1}{2}}C_R^b}\right)$$

where R is ideal gas constant, T is absolute temperature, n is the number of electron transferred, F is Faraday's constant, A is the area of the electrode, $D_O$ and $D_R$ are the

diffusivity of oxidation and reduction species, respectively. Then $C_O$ and $C_R$ are the concentration of oxidation and reduction species, respectively. In addition, because of the fact that only $Li^+$ which moving inside of graphite electrode, the Warburg coefficient ($\sigma$) can be simplified by :

$$\sigma = \frac{RT}{n^2F^2A\sqrt{2}}\left(\frac{1}{D_{Li}^{1/2}C_{Li}}\right)$$

where $D_{Li}$ and $C_{Li}$ are the diffusion coefficient and concentration of $Li^+$.

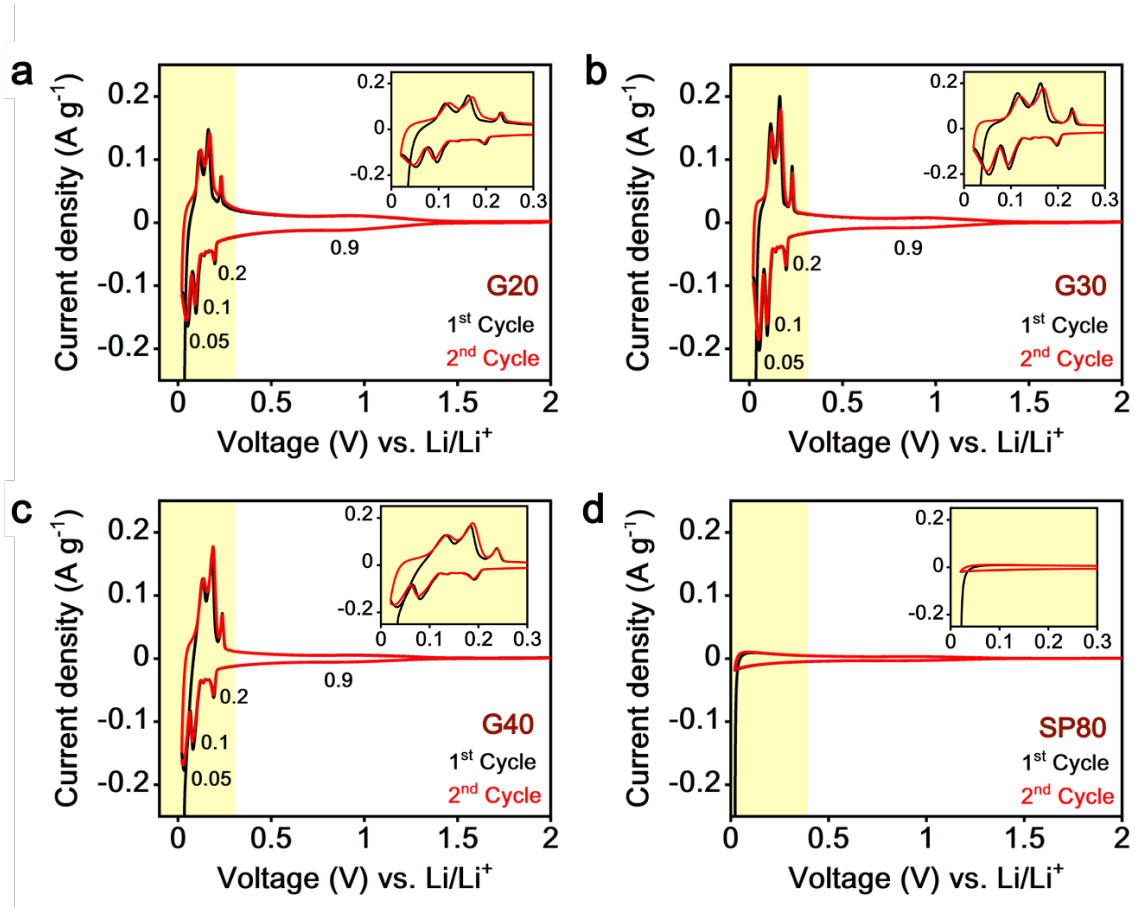


Fig. S1. The cyclic voltammogram of: (a) **G20**; (b) **G30**; (c) **G40** and (d) **SP80**. The inset figure is the zoom in on the highlighted region.

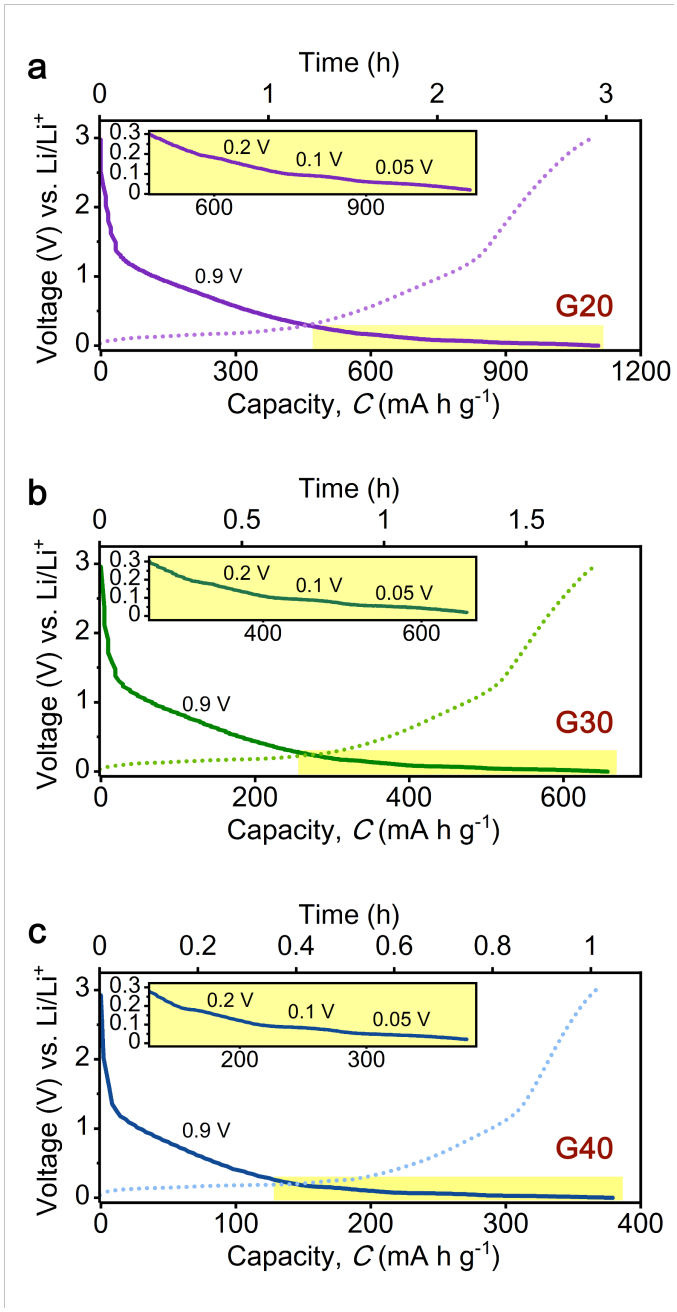


Fig. S2. The Galvanostatic charge/discharge profile of: (a) **G20**; (b) **G30**; and (c) **G40** at selected 100$^{th}$ charge/discharge under 1C. The inset figure is the zoom in on the highlighted region.

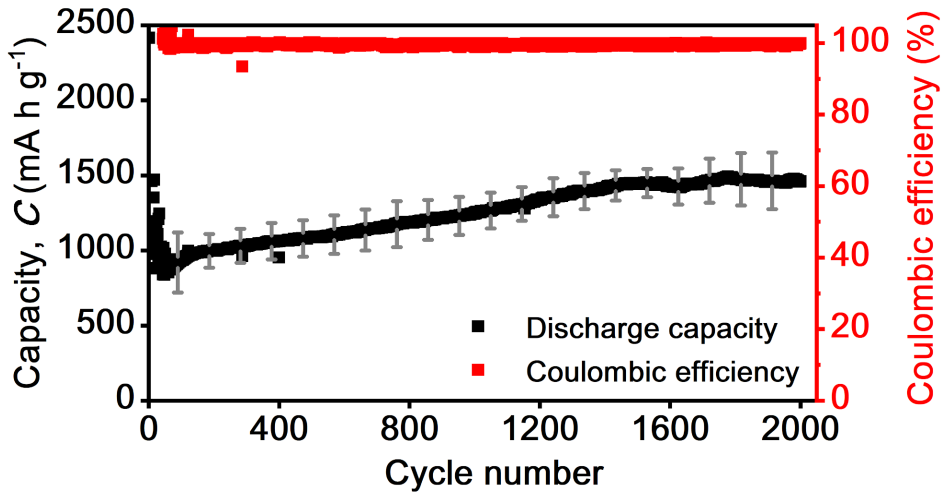


Fig. S3. The capacity profile and Coulombic efficiency of **G10** at 30C.

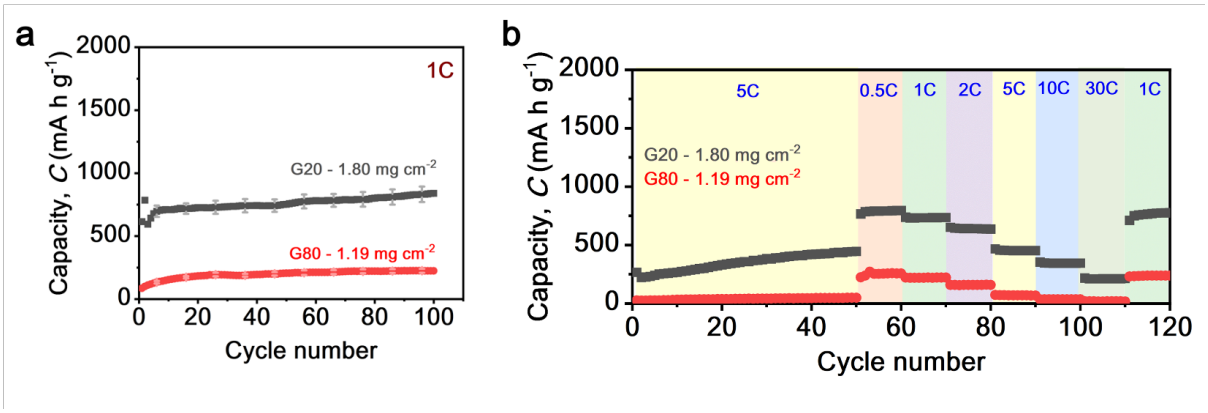


Fig. S4. The electrochemical performance of **G20** and **G80** with closer active material loading. (a) Cycling performance at 1C rate. (b) Rate performance analysis.

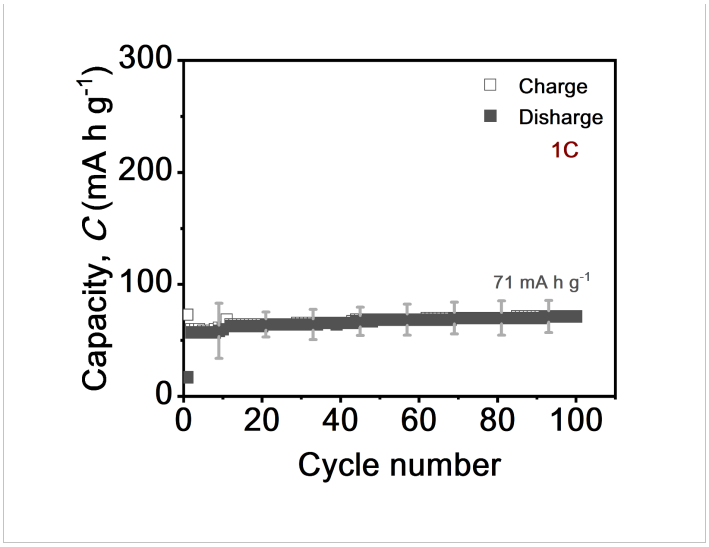


Fig. S5. The electrochemical performance of **SP80** a at 1C rate.

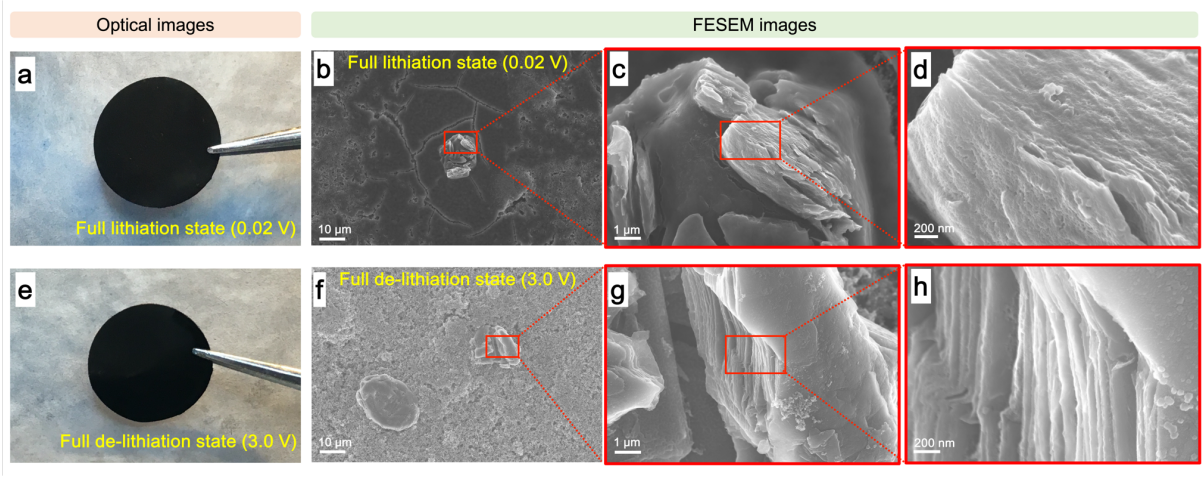


Fig. S6. The optical and field emission scanning electron microscope (FESEM) images of **G20** at full lithiation (0.02 V) and de-lithiation state (3.0 V) at 1C. (a&e) is the optical images; (b – d) and (f – h) is the FESEM images with different magnification at full lithiation (0.02 V) and de-lithiation state (3.0 V), respectively.

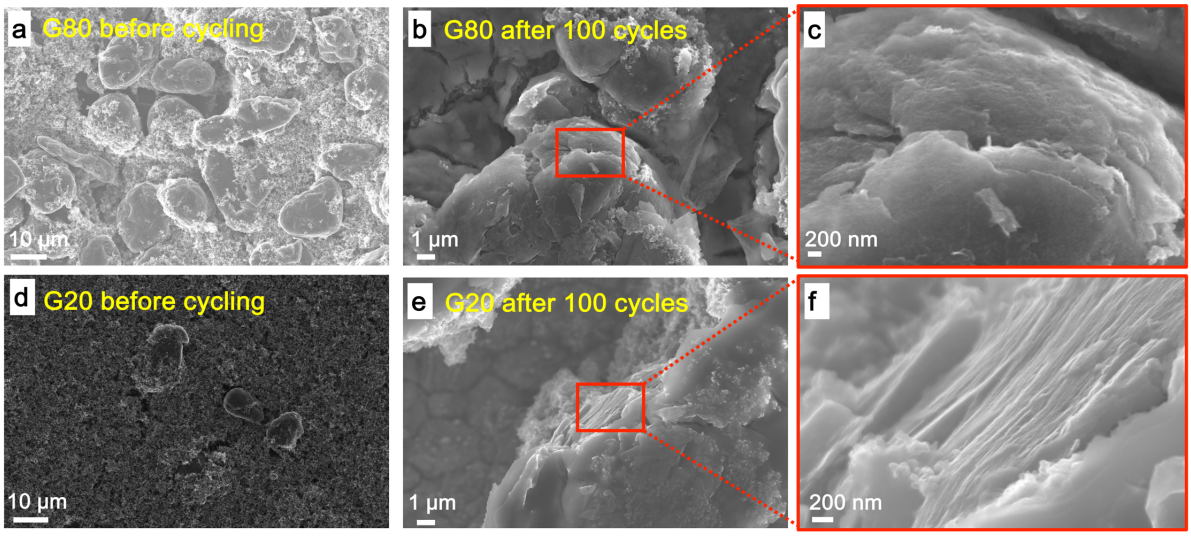


Fig. S7. The FESEM images before and after 100 cycles at 1C rate. (a&d) is **G80** and **G20** before cycling; (b&c) and (e&f) are **G80** and **G20** after 100 cycles at different magnification, respectively.

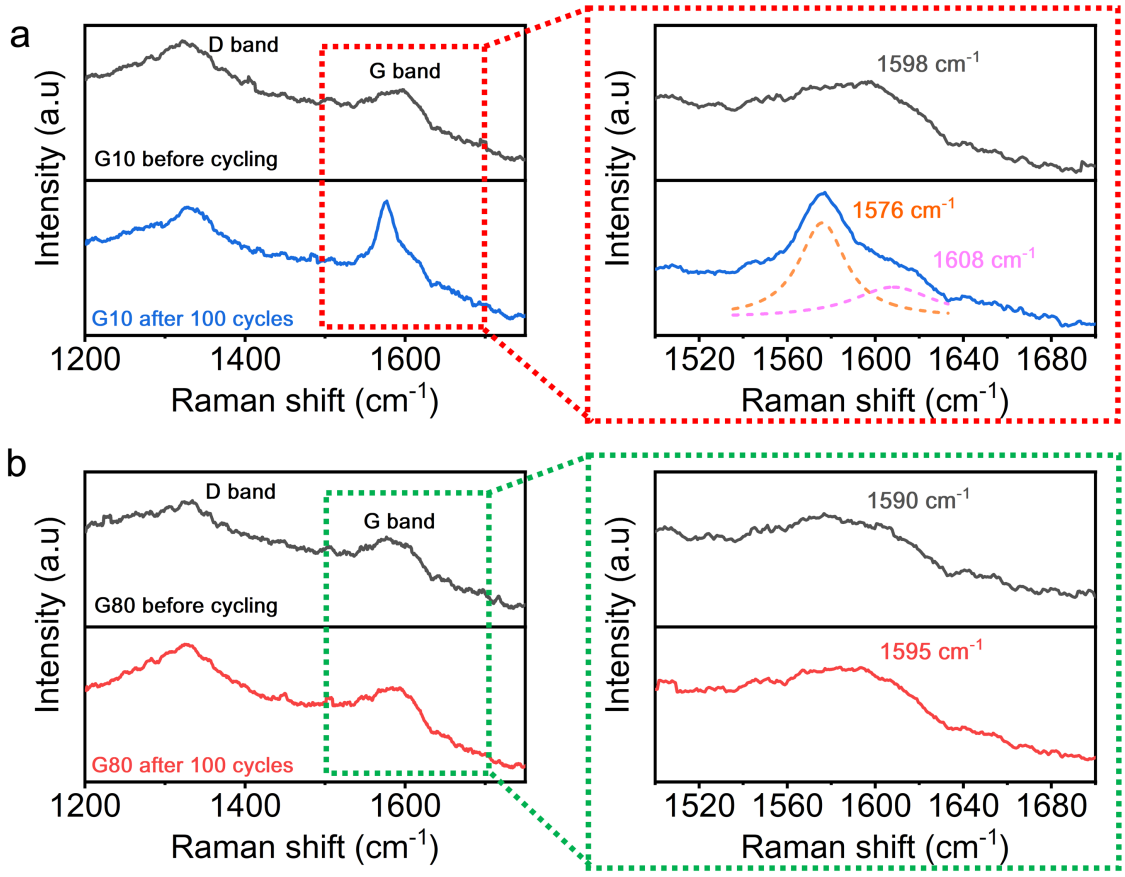


Fig. S8. Raman spectra of **G10** (a) and **G80** (b) at before and after 100 cycles at 1C with the highlighted area of G band.

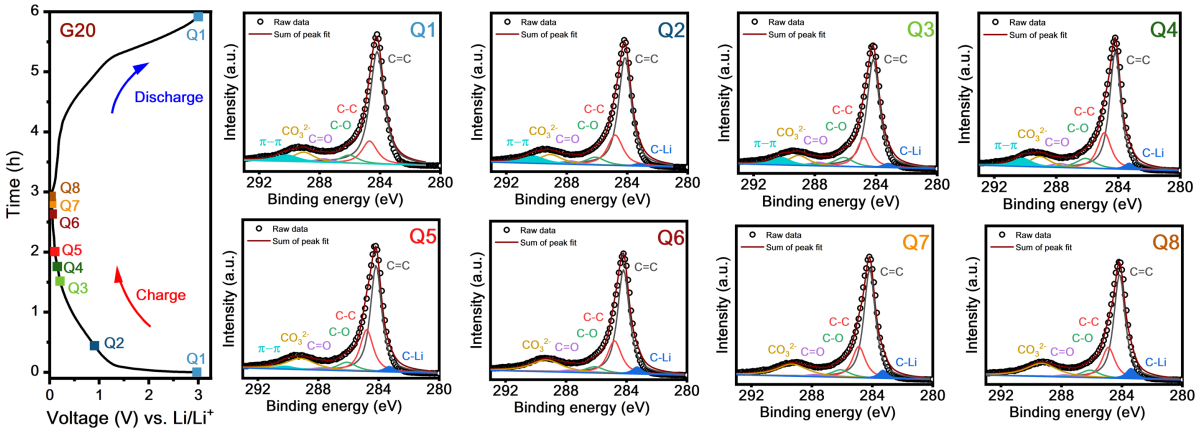


Fig. S9. The C1s ex-situ XPS spectra analysis of **G20** at selected states on the 2nd charge-discharge process. (Q1: initial state at 3.0 V; Q2: charged state at 0.9 V; Q3: charged state at 0.2 V; Q4: charged state at 0.15 V; Q5: charged state at 0.1 V; Q6: charged state at 0.05 V; Q7: charged state at 0.03 V; Q8: charged state at 0.02 V). This analysis have been summarized in Fig. 2d.

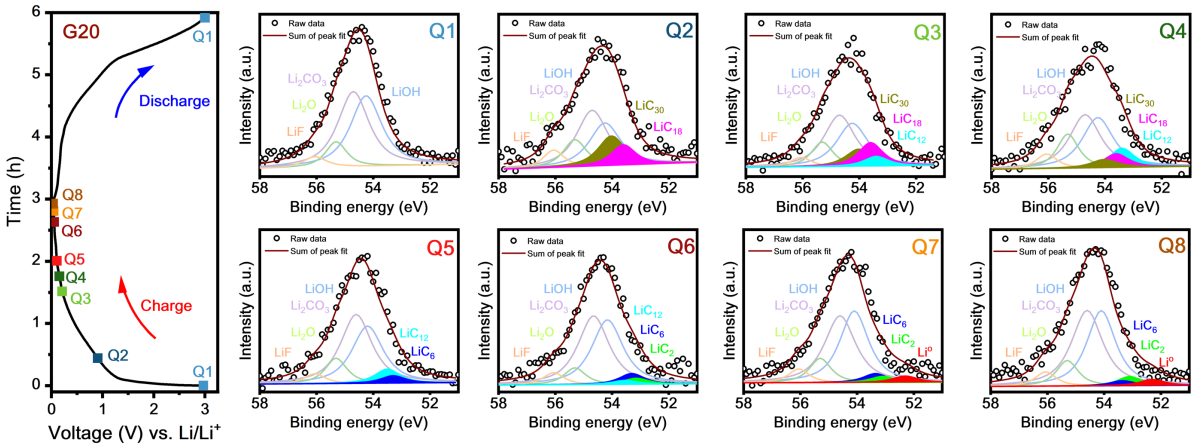


Fig. S10. The Li1s ex-situ XPS spectra analysis of **G20** at selected states on the 2nd charge-discharge process. (Q1: initial state at 3.0 V; Q2: charged state at 0.9 V; Q3: charged state at 0.2 V; Q4: charged state at 0.15 V; Q5: charged state at 0.1 V; Q6: charged state at 0.05 V; Q7: charged state at 0.03 V; Q8: charged state at 0.02 V). This analysis have been summarized in Fig. 2e – 2f.

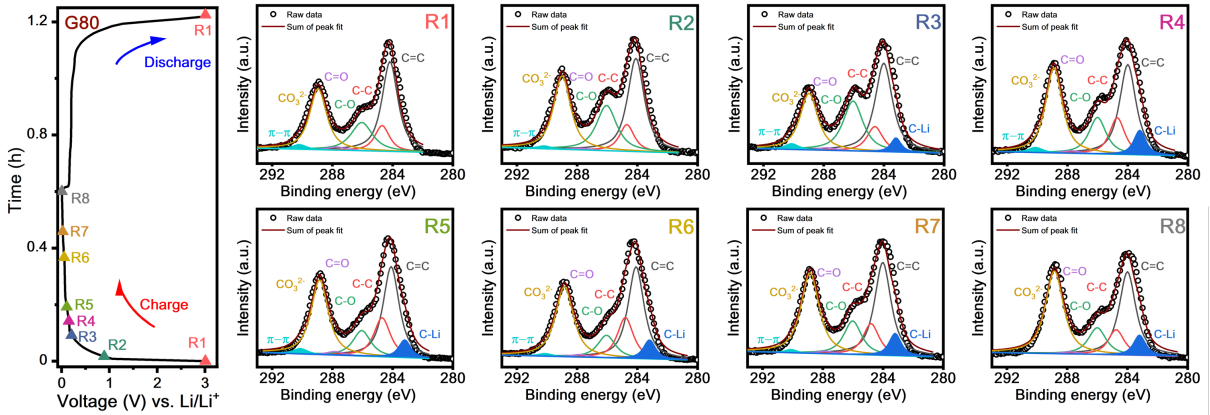


Fig. S11. The C1s ex-situ XPS spectra analysis of **G80** at selected states on the 2nd charge-discharge process. (R1: initial state at 3.0 V; R2: charged state at 0.9 V; R3: charged state at 0.2 V; R4: charged state at 0.15 V; R5: charged state at 0.1 V; R6: charged state at 0.05 V; R7: charged state at 0.03 V; R8: charged state at 0.02 V). This analysis have been summarized in Fig. 2h.

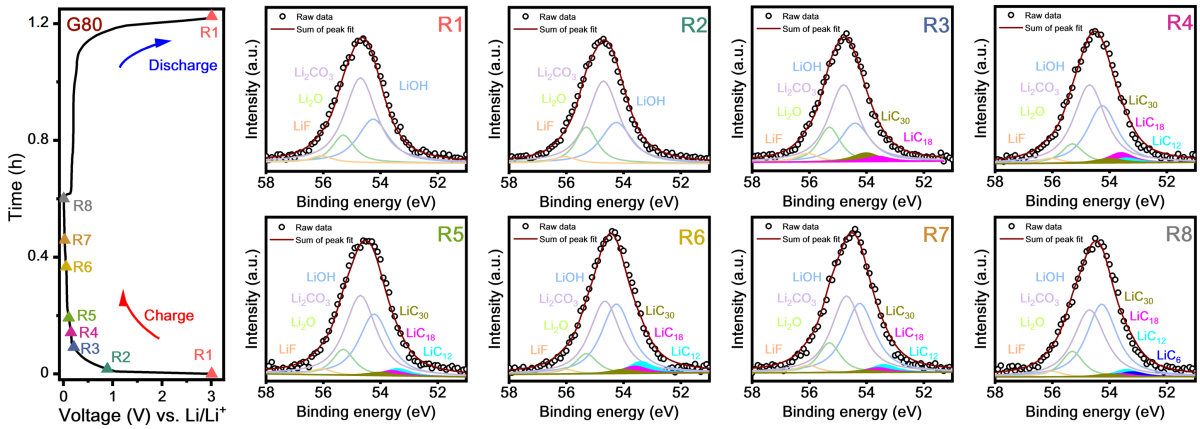


Fig. S12. The Li1s ex-situ XPS spectra analysis of **G80** at selected states on the 2nd charge-discharge process. (R1: initial state at 3.0 V; R2: charged state at 0.9 V; R3: charged state at 0.2 V; R4: charged state at 0.15 V; R5: charged state at 0.1 V; R6: charged state at 0.05 V; R7: charged state at 0.03 V; R8: charged state at 0.02 V). This analysis have been summarized in Fig. 2i – 2j.

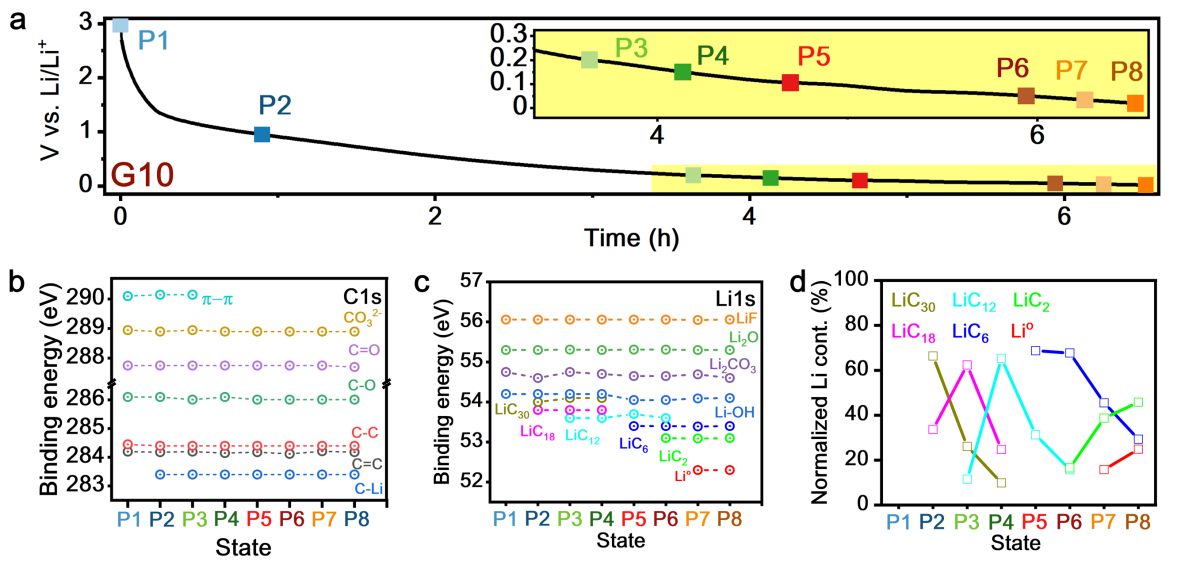


Fig. S13. The ex-situ XPS spectra analysis of **G10** at selected states on the 2nd charge-discharge process. (a) Selected states of *ex-situ* XPS analysis on the **G10** during charge process, namely P1: initial state at 3.0 V; P2: charged state at 0.9 V; P3: charged state at 0.2 V; P4: charged state at 0.15 V; P5: charged state at 0.1 V; P6: charged state at 0.05 V; P7: charged state at 0.03 V; P8: charged state at 0.02 V. (b) and (c) C1s and Li1s XPS spectra of **G10** shown at various charge stages. (d) Normalized $Li^+$ content in **G10** at different charge stages.

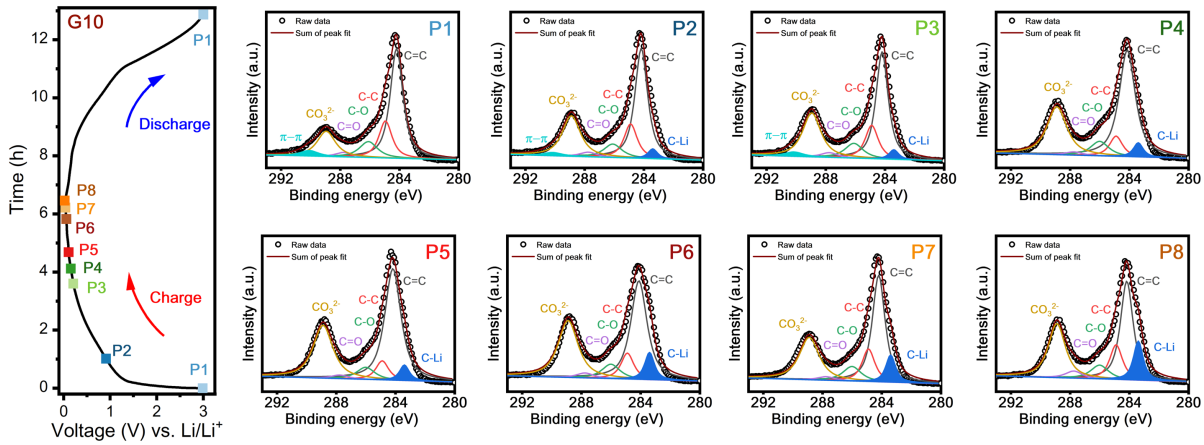


Fig. S14. The C1s ex-situ XPS spectra analysis of **G10** at selected states on the 2nd charge-discharge process. (P1: initial state at 3.0 V; P2: charged state at 0.9 V; P3: charged state at 0.2 V; P4: charged state at 0.15 V; P5: charged state at 0.1 V; P6: charged state at 0.05 V; P7: charged state at 0.03 V; P8: charged state at 0.02 V). This analysis have been summarized in Fig. S13b.

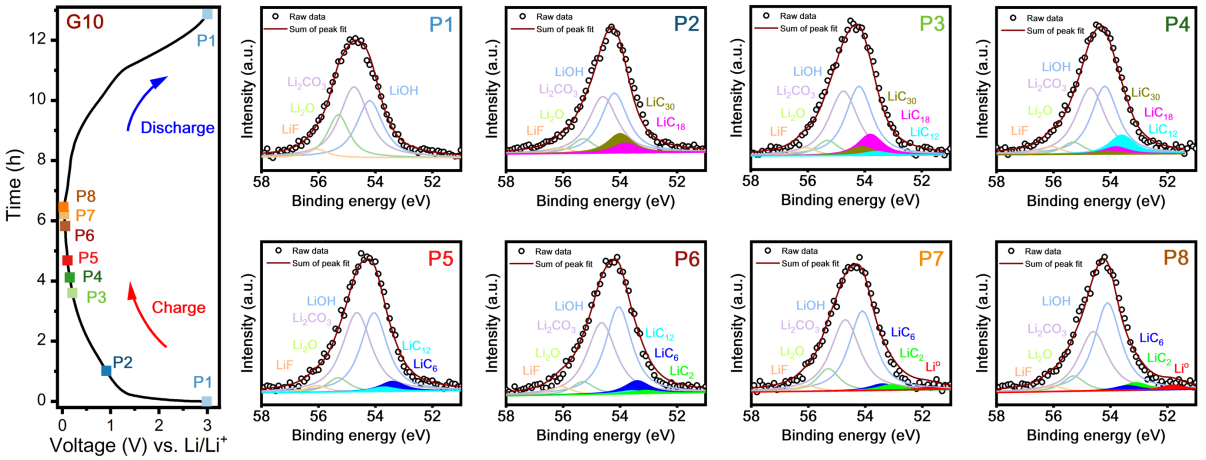


Fig. S15. The C1s ex-situ XPS spectra analysis of **G10** at selected states on the 2nd charge-discharge process. (P1: initial state at 3.0 V; P2: charged state at 0.9 V; P3: charged state at 0.2 V; P4: charged state at 0.15 V; P5: charged state at 0.1 V; P6: charged state at 0.05 V; P7: charged state at 0.03 V; P8: charged state at 0.02 V). This analysis have been summarized in Fig. S13c – d.

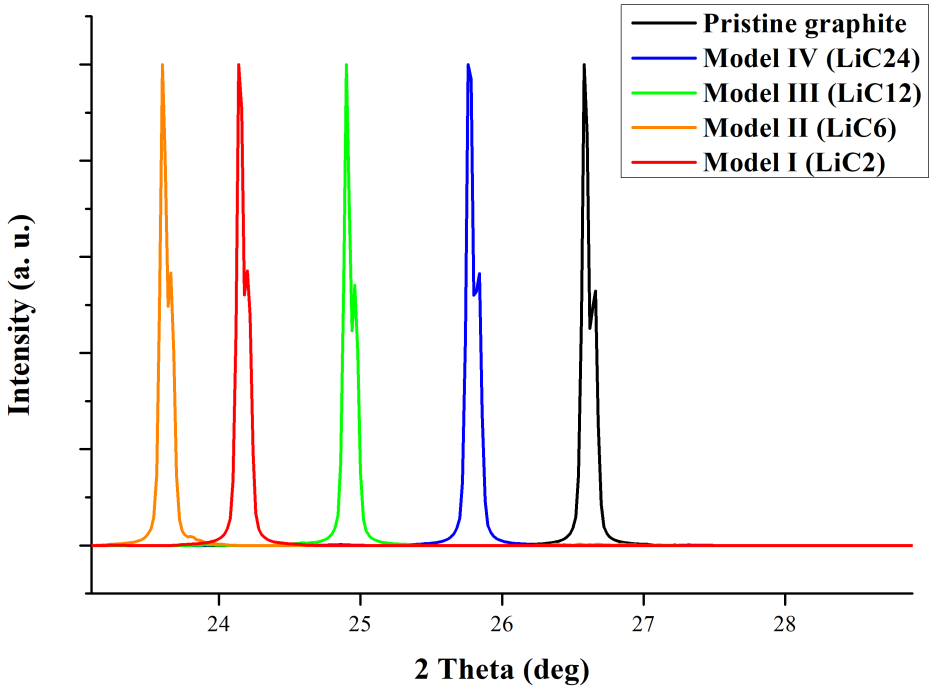


Fig. S16. The calculating X-Ray Diffraction (XRD) spectrum of pristine graphite and lithiated graphite of Model I-IV.

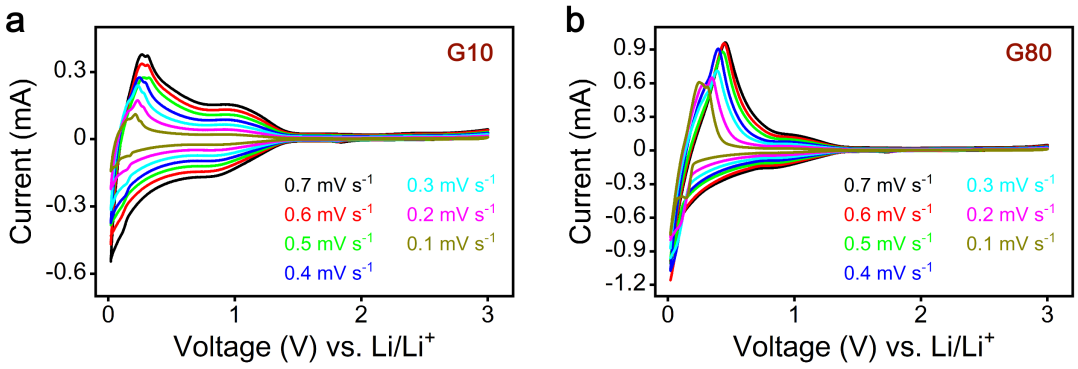


Fig. S17. The sweep rate CV of **G10** (a) and **G80** (b) at different scan rate.

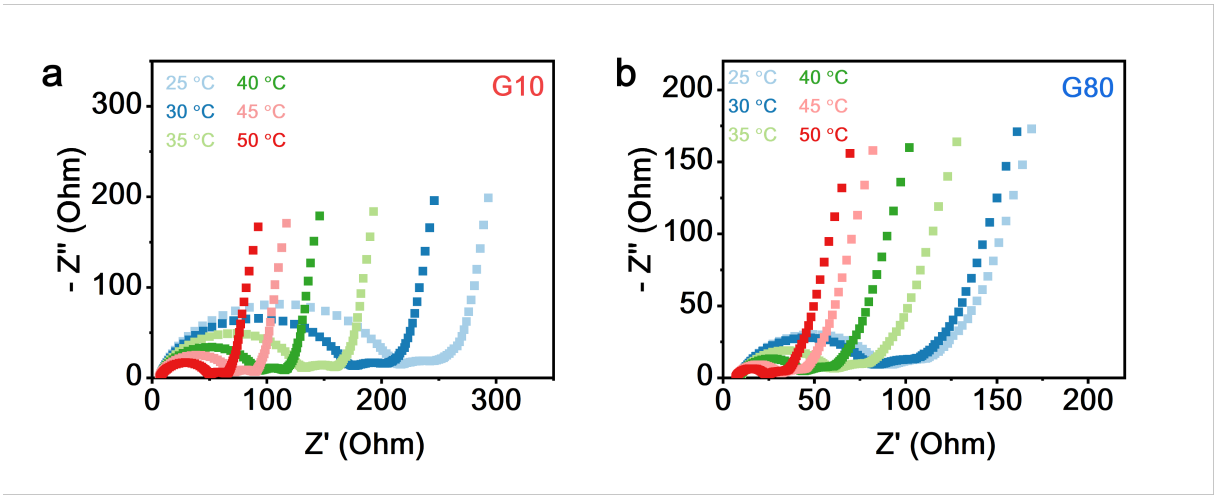


Fig. S18. The Nyquist plot of **G10** (a) and **G80** (b) at various temperatures.

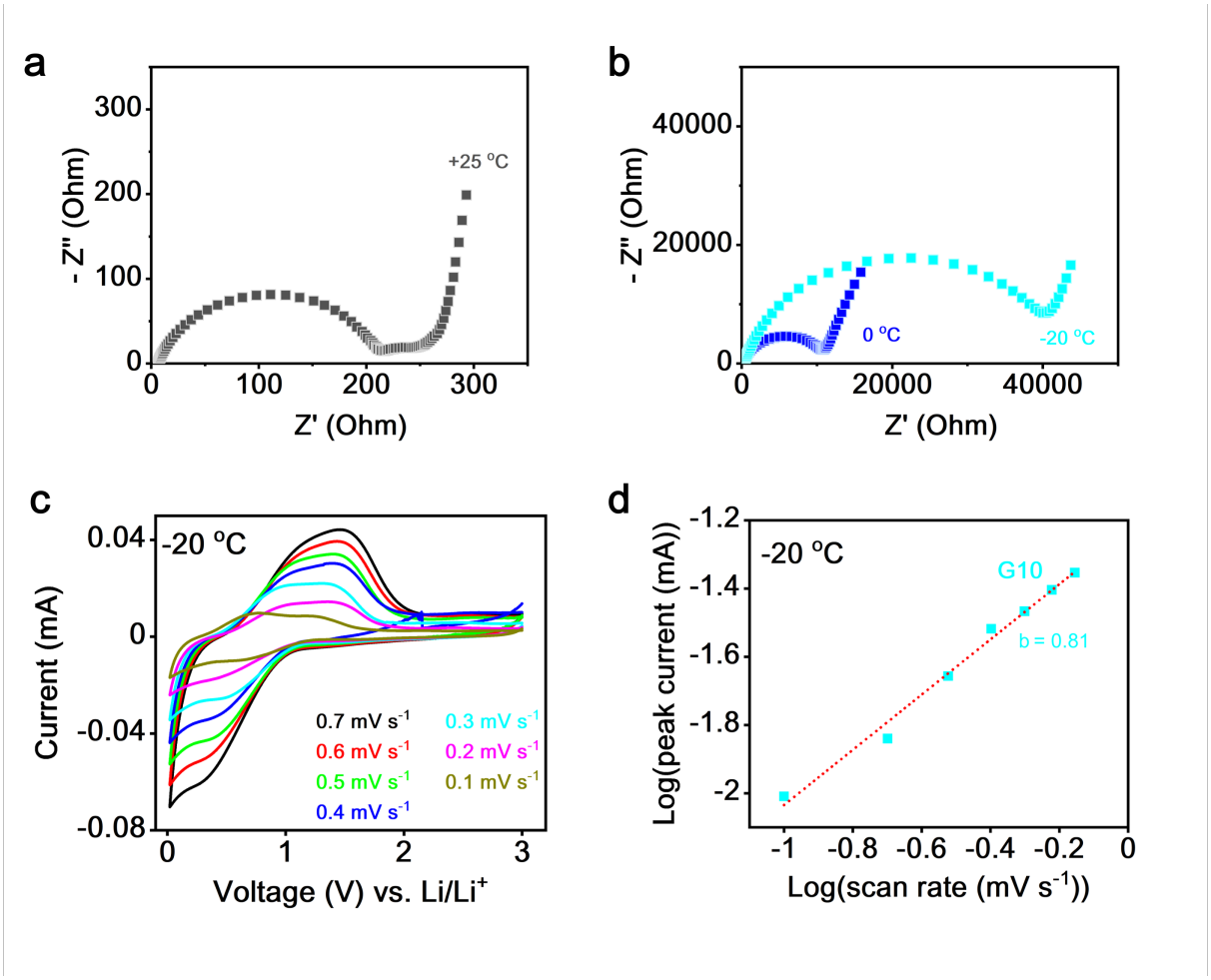


Fig. S19. (a) and (b) Nyquist plots of **G10** at different temperature. (c) The sweep rate CV **G10** at -20 °C. (d) The *b* value as slope function of Log scan rate (*v*) vs Log peak current (*i*) for **G10** at -20 °C.

Table S1. The adsorption energies ($E_{ad}$), averaged interlayer distance ($d_{avg}$) and theoretical capacities of Model I-IV.

| Model | $E_{ad}$ (eV/Li atom) | $d_{avg}$ (Å) | Theoretical capacity (mA h $g^{-1}$) |
|---|---|---|---|
| Pristine graphite | - | 3.348 | - |
| Model IV ($LiC_{24}$) | -1.778 | 3.454 | 93 |
| Model III ($LiC_{12}$) | -1.853 | 3.668 | 186 |
| Model II ($LiC_6$) | -1.867 | 3.767 | 372 |
| Model I ($LiC_2$) | -1.734 | 3.682 | 1116 |

Table S2. Summary of LIBs operated at low-temperatures.

| Electrode | Electrolyte | Temp. (ºC) | Current density (mA $g^{-1}$) | Cycling performance (mA h $g^{-1}$) | ref |
|---|---|---|---|---|---|
| Oxidized graphite | 1M $LiPF_6$ EC:DEC:DMC | -20 | 0.5 C (1C: 372 mA h $g^{-1}$) | 223 | 14 |
| Ag-graphite | | -20 | | 242 | |
| Al-graphite | | -20 | | 245 | |
| Cu-graphite | | -20 | | 149 | |
| $Li_4Ti_5O_{12}$ | 1 M $LiPF_6$ PC:DME | 0 | 0.125 C | 145 | 15 |
| | | -20 | | 115 | |
| | | -30 | | 82 | |
| $Li_4Ti_5O_{12}$/C | 1 M $LiPF_6$ EC:DMC | 0 | 1 C | 145 | 16 |
| | | -10 | | 125 | |
| | | -20 | | 119 | |
| Fluoride-doped $Li_4Ti_5O_{12}$ | 1 M $LiPF_6$ EC:EMC | -10 | 175 | 130 | 17 |
| | | -20 | 175 | 100 | |
| $Li_4Ti_5O_{12}$-$TiO_2$ composite | 1M $LiPF_6$ EC:DMC:EMC | -10 | 175 | 135 | 18 |
| | | -20 | 175 | 129 | |
| | | -30 | 175 | 118 | |
| Sn-coated graphite | 1M $LiPF_6$ EC:DEC:DMC | 0 | 0.5 C | 357 | 19 |
| | | -10 | | 342 | |
| | | -20 | | 273 | |
| | | -30 | | 152 | |
| Nano-Sn/expanded graphite | 1 M $LiPF_6$ EC:DMC | 25 | 65 | 650 | 20 |
| | | -20 | 65 | 200 | |
| | | -20 | 130 | 130 | |
| 3D porous Cu-Zn alloy | 1 M $LiPF_6$ EC:DMC | -10 | 100 | 250 | 21 |
| | | -20 | 100 | 200 | |
| | | -30 | 100 | 150 | |
| $Cu_2ZnSnS$ | 1M $LiPF_6$ EC:DEC:DMC | -10 | 500 | 475 | 22 |

| | | | | | |
|---|---|---|---|---|---|
| | 1M $LiPF_6$ EC:DEC | -10 | 500 | 372 | |
| $MoS_2$/C | 1 M $LiPF_6$ EC:DMC | -20 | 100 | 854 | 23 |
| | | -20 | 3000 | 140 | |
| Mesoporous/Ge | 1.3 M $LiPF_6$ EC:DEC | -20 | 85 | 566 | 24 |
| N-doped graphite | 1 M $LiBF_4$ EC:DEC:DMC | -10 | 0.1 C | 225 | 25 |
| Graphydine | 1M $LiPF_6$ EC:DEC:DMC + 2wt% VC | 0 | 2 C (1C= 744 mA h $g^{-1}$) | 380 | 26 |
| | | -10 | 2 C | 268 | |
| | | -10 | 4 C | 132 | |
| Ultra-low graphite content electrode (**G10**) | 1 M $LiPF_6$ EC:DEC | 0 | 1 C | 1250 | **This work** |
| | | -20 | 1 C | 1100 | |

**Supplementary references:**


1. J. Wang, J. Polleux, J. Lim and B. Dunn, *J. Phys. Chem. C*, 2007, **111**, 14925-14931.
2. F.-F. Li, J.-F. Gao, Z.-H. He and L.-B. Kong, *ACS Appl. Energy Mater.*, 2020, **3**, 5448-5461.
3. V. Augustyn, J. Come, M. A. Lowe, J. W. Kim, P.-L. Taberna, S. H. Tolbert, H. D. Abruña, P. Simon and B. Dunn, *Nat. Mater.*, 2013, **12**, 518-522.
4. F. Yu, Z. Liu, R. Zhou, D. Tan, H. Wang and F. Wang, *Mater. Horiz.*, 2018, **5**, 529-535.
5. H. Lindström, S. Södergren, A. Solbrand, H. Rensmo, J. Hjelm, A. Hagfeldt and S.-E. Lindquist, *J. Phys. Chem. B*, 1997, **101**, 7717-7722.
6. T. C. Liu, *J. Electrochem. Soc.*, 1998, **145**, 1882.
7. T. Q. Nguyen and C. Breitkopf, *J. Electrochem. Soc.*, 2018, **165**, E826-E831.
8. T. Osaka, T. Momma, D. Mukoyama and H. Nara, *J. Power Sources*, 2012, **205**, 483-486.
9. H.-M. Cho, W.-S. Choi, J.-Y. Go, S.-E. Bae and H.-C. Shin, *J. Power Sources*, 2012, **198**, 273-280.
10. S. Rodrigues, N. Munichandraiah and A. K. Shukla, *J. Solid State Electrochem.*, 1999, **3**, 397-405.
11. E. Barsoukov and J. R. Macdonald, *Impedance Spectroscopy: Theory, Experiment, and Applications*, Wiley, 2018.
12. D. Aurbach, B. Markovsky, M. D. Levi, E. Levi, A. Schechter, M. Moshkovich and Y. Cohen, *J. Power Sources*, 1999, **81-82**, 95-111.
13. A. J. Bard and L. R. Faulkner, *Electrochemical Methods: Fundamentals and Applications, 2nd Edition*, Wiley Textbooks, 2000.
14. F. Nobili, S. Dsoke, T. Mecozzi and R. Marassi, *Electrochim. Acta*, 2005, **51**, 536-544.
15. J. L. Allen, T. R. Jow and J. Wolfenstine, *J. Power Sources*, 2006, **159**, 1340-1345.
16. T. Yuan, X. Yu, R. Cai, Y. Zhou and Z. Shao, *J. Power Sources*, 2010, **195**, 4997-5004.
17. Y. Zhang, Y. Luo, Y. Chen, T. Lu, L. Yan, X. Cui and J. Xie, *ACS Appl. Mater. Interfaces*, 2017, **9**, 17145-17154.

18. C. Huang, S.-X. Zhao, H. Peng, Y.-H. Lin, C.-W. Nan and G.-Z. Cao, *J. Mater. Chem. A*, 2018, **6**, 14339-14351.
19. F. Nobili, M. Mancini, S. Dsoke, R. Tossici and R. Marassi, *J. Power Sources*, 2010, **195**, 7090-7097.
20. Y. Yan, L. Ben, Y. Zhan and X. Huang, *Electrochim. Acta*, 2016, **187**, 186-192.
21. A. Varzi, L. Mattarozzi, S. Cattarin, P. Guerriero and S. Passerini, *Adv. Energy Mater.*, 2018, **8**, 1701706.
22. Z. Syum, T. Billo, A. Sabbah, B. Venugopal, S.-Y. Yu, F.-Y. Fu, H.-L. Wu, L.-C. Chen and K.-H. Chen, *ACS Sustain. Chem. Eng.*, 2021, **9**, 8970-8979.
23. X. Liu, Y. Wang, Y. Yang, W. Lv, G. Lian, D. Golberg, X. Wang, X. Zhao and Y. Ding, *Nano Energy*, 2020, **70**, 104550.
24. S. Choi, Y.-G. Cho, J. Kim, N.-S. Choi, H.-K. Song, G. Wang and S. Park, *Small*, 2017, **13**, 1603045.
25. F. Lu, J. Liu, J. Xia, Y. Yang and X. Wang, *Ind. Eng. Chem. Res.*, 2020, **59**, 5858-5864.
26. J. An, H. Zhang, L. Qi, G. Li and Y. Li, *Angew. Chem. Int. Ed.*, 2022, **61**, e202113313.